Fan et al.
EURASIP Journal on Advances in Signal Processing (2024) 2024:39
https://doi.org/10.1186/s13634-024-01137-z

EURASIP Journal on Advances
in Signal Processing

RESEARCH

Open Access

Improved reliable high-order SPECAN algorithm for highly squinted SAR imaging processing

Wenna Fan[1*], Yang Bi[1] and Min Zhang[2]

*Correspondence:
201906006@xaau.edu.cn

[1] School of Electronic Engineering, Xi'an Aeronautical Institute, Xi'an 710077, China
[2] School of Physics, Xidian University, Xi'an 710071, China

Abstract

For the processing of highly squinted synthetic aperture radar (SAR) echo signals, three key challenges need to be considered: rectifying the nonzero Doppler centroid, compensating for azimuthal side-lobe defocusing (ASLD), and correcting the range cell migration (RCM). To address these three problems, we developed a reliable improved fourth-order spectral analysis (SPECAN) algorithm for highly squinted SAR imaging in this study. First, we present a fourth-order phase model (FoPM) that is more suitable for the highly squinted SAR system through a theoretical analysis. Second, based on the FoPM, we derive an improved fourth-order SPECAN algorithm in detail. In this derivation, the nonzero Doppler centroid, the ASLD, and the RCM caused by the high squint angle are corrected. Moreover, the whole simulation procedure of the improved algorithm only contains fast Fourier transform and complex multiplication, so the proposed algorithm can efficiently process highly squinted SAR echoes. Furthermore, the results of a comparison with the traditional SPECAN algorithm show the better performance of the proposed algorithm.

Keywords: SPECAN algorithm, Synthetic aperture radar, Highly squinted

1 Introduction

Because of its capability to provide two-dimensional high-resolution images of a scene of interest in all weather, all day, and all night, synthetic aperture radar (SAR) has been widely used as a powerful remote sensing tool in both the military and civilian fields [1, 2]. For further applications, SAR systems are increasingly being mounted on maneuvering platforms [3–10] for disaster monitoring, terrain detection, etc. Compared with the general side-look SAR, a squinted SAR works in a high-squint mode to obtain a period of turning time. To improve the ability of a highly squinted SAR for the detection and recognition of targets, a reliable method for processing the received echo signals is necessary.

Many imaging algorithms have been proposed for processing low squinted SAR echoes. The range Doppler algorithm is a common basic imaging algorithm, but it needs an interpolation operation and can handle only about a squint angle less than 10°, so it cannot meet the requirements of highly squinted SAR imaging [11]. The chirp scaling (CS) algorithm [12] is well-known in the study of squinted SAR imaging: It firstly removes the range walk in time domain, and then the unified range cell migration correction (RCMC) is accurately performed by the CS operation. However, the CS algorithm does not consider the effect of high-order range curvature in the azimuth direction. Thus, with the increase in squint angle, it is unable to obtain a well-focused SAR image. The nonlinear CS algorithm [13] and its improved algorithm [14, 15] can be used to deal with highly squinted echoes, but they both have high computational complexity and low computational efficiency. The spectral analysis (SPECAN) algorithm [16, 17] is highly efficient, but only corrects the public linear parts of range cell migration (RCM). When applied to highly squinted SAR imaging, the approximation error of the azimuth phase increases with the squint angle. As a result, an SAR image with low accuracy in highly squinted cases is produced, so it is mostly used in medium or low squint cases.

To simulate highly squinted SAR images, three main problems must be solved: First, the nonzero Doppler centroid leads to Doppler ambiguity. Second, high-order phase errors need to be considered; otherwise, azimuthal side-lobe defocusing (ASLD) will occur. Third, the serious coupling between the azimuth and range directions results in a spatial-variant RCM. Considering the above three problems, further research is required on the highly squinted SAR imaging algorithm. Consequently, based on the previous studies, we constructed an improved SPECAN algorithm that extends the azimuth phase of the echo signal to the fourth order to process highly squinted SAR echo data. The proposed model not only removes the impact of squint angle on ASLD, but also mitigates the significant spatial-variant RCM. That is, together with the improved SPECAN algorithm, the highly squinted SAR echo can be processed to produce a well-focused SAR image.

We further used the proposed algorithm used to process an SAR echo from a complex target. To generate a highly squinted SAR echo of targets, the key point is the accurate estimation of the scattering properties of targets. We used the geometrical optics and physical optics (GO-PO) hybrid method [18–20] to analyze the electromagnetic scattering from targets because of its high efficiency and accuracy.

The remainder of this paper is organized as follows: Section 2 presents a brief description of the imaging geometry in highly squinted SAR, and the impacts of squint angle on azimuth phase error are analyzed. Section 3 provides a detailed derivation of the improved SPECAN algorithm. Then, the validity of the proposed algorithm is demonstrated through a comparison with the traditional SPECAN method in Sec. 4. In addition, we applied the algorithm to simulate the highly squinted SAR image of an airplane target and a composite ship-ocean scene to further verify its effectiveness. Some conclusions are provided in Sec. 5.

2 Highly squinted SAR geometry and phase error analysis

2.1 Highly squinted geometry and signal model

Due to the high speed of a SAR platform, the nonlinear motion of a SAR can be approximated as a linear motion in a relatively short period of time. As illustrated in Fig. 1a, suppose an SAR is flying at a constant speed v at a height H along the positive y-axis. During data acquisition, the SAR beam illuminates the target of interest with a squint angle of θ_s. In Fig. 1, R_0 denotes the vertical distance between the scene center

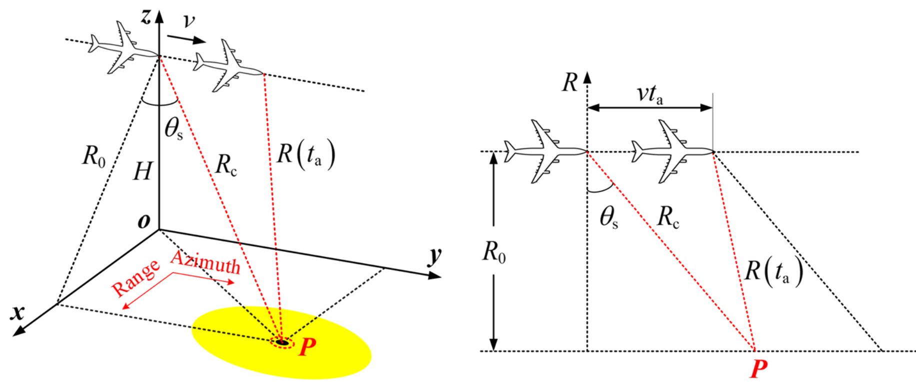

Fig. 1 Imaging geometry: (**a**) geometrical model of highly squinted SAR imaging; (**b**) the slant-range plane of (**a**)

point P and the flight path. At azimuth time $t_a = 0$, the slant range between the beam center and the point P is R_c. Figure 1b depicts the slant-range plane of Fig. 1a. Then, the expression of the instantaneous slant range $R(t_a)$ between the SAR platform and the point P at t_a is:

$$R(t_a) = \sqrt{(vt_a)^2 + R_c^2 - 2R_c vt_a \sin\theta_s} \tag{1}$$

Assuming that a linear frequency modulation signal is transmitted by the SAR with a central frequency of f_c, the received echo signal $S_s(t_a, t_r)$ from an arbitrary target is:

$$\begin{aligned} S_s(t_a, t_r) &= w_a(t_a) w_r\left[t_r - 2\frac{R(t_a)}{c}\right]\sigma(\theta_i, \theta_a) \\ &\cdot \exp\left[-j4\pi f_c \frac{R(t_a)}{c}\right]\exp\left[j\pi K_r\left(t_r - 2\frac{R(t_a)}{c}\right)^2\right] \end{aligned} \tag{2}$$

where $w_a(t_a)$ and $w_r(t_r)$ are the azimuth and range envelops, respectively; t_r is the range time; c is the speed of light; $\sigma(\theta_i, \theta_a)$ is the backscattering coefficient with incident angle θ_i and azimuth angle θ_a; j = $\sqrt{-1}$ is the imaginary unit; and K_r is the range chirp rate.

2.2 Phase error analysis

Equation (1) can be rewritten as Eq. (3) by the Taylor series expansion with respect to $t_a = 0$:

$$\begin{aligned} R(t_a) &= R_c + \gamma_1(R_c)t_a + \gamma_2(R_c)t_a^2 + \gamma_3(R_c)t_a^3 + \gamma_4(R_c)t_a^4 + \cdots \\ &= R_c - \lambda f_{dc}\frac{t_a}{2} - \lambda f_{dr}\frac{t_a^2}{4} + \gamma_3(R_c)t_a^3 + \gamma_4(R_c)t_a^4 + \cdots \end{aligned} \tag{3}$$

where the linear term is called the linear range walk (LRW), the quadratic term and other higher-order terms are called the range curvature. The LRW and range curvature together constitute the total RCM. $\gamma_1(R_c)$, $\gamma_2(R_c)$, $\gamma_3(R_c)$, and $\gamma_4(R_c)$ are the coefficient of

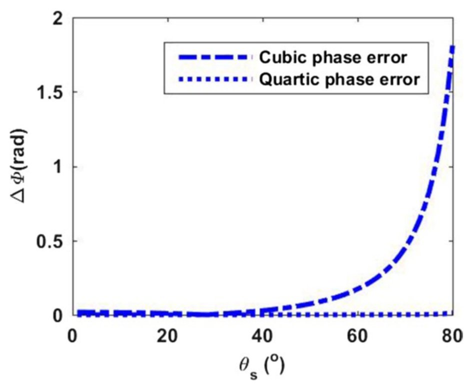

Fig. 2 Variation in phase error with squint angle

Table 1 Simulation parameters

Parameter	Value
Squint angle	80°
Radar platform speed	1020 m/s
Carrier frequency	15 GHz
Transmitted bandwidth	80 MHz
Pulse width	2 μs
Height	3000 m
Antenna size	3 m

each term. The second row in Eq. (3) shows that the instantaneous slant range is related to the Doppler centroid f_{dc} and Doppler rate f_{dr} [21, 22], where $\lambda = \frac{c}{f_c}$ is the center wavelength.

According to Eq. (2), the azimuth phase of the echo signal is:

$$\phi_{\mathrm{a}} = -4\pi f_{\mathrm{c}} \frac{R(t_{\mathrm{a}})}{\mathrm{c}} \tag{4}$$

Then, by substituting Eq. (3) into (4), the cubic phase $\phi_{3\mathrm{a}}$ and the quartic phase $\phi_{4\mathrm{a}}$ can be expressed as:

$$\phi_{3\mathrm{a}} = -4\pi f_{\mathrm{c}} \frac{\left[R_{\mathrm{c}} + \gamma_1(R_{\mathrm{c}})t_{\mathrm{a}} + \gamma_2(R_{\mathrm{c}})t_{\mathrm{a}}^2 + \gamma_3(R_{\mathrm{c}})t_{\mathrm{a}}^3\right]}{\mathrm{c}} \tag{5}$$

$$\phi_{4\mathrm{a}} = \phi_{3\mathrm{a}} - 4\pi f_{\mathrm{c}} \frac{\gamma_4(R_{\mathrm{c}})}{\mathrm{c}} t_{\mathrm{a}}^4 \tag{6}$$

Together with Eqs. (4), (5), and (6), the cubic and quartic phase errors are, respectively:

$$\Delta\Phi_{3\mathrm{a}} = |\phi_{\mathrm{a}} - \phi_{3\mathrm{a}}| \tag{7}$$

$$\Delta\Phi_{4\mathrm{a}} = |\phi_{\mathrm{a}} - \phi_{4\mathrm{a}}| \tag{8}$$

Figure 2 shows the simulation results of the cubic and quartic phase errors for squint angles from 0° to 80°, and the SAR parameters are listed in Table 1. From the simulation result, we found that in side-looking or low-squint mode, the cubic phase error is low; namely, the fourth-order and higher-order terms have little impact on the imaging results. However, when the squint angle is larger than 40°, the cubic phase error substantially increases with increasing squint angle. That is, the Taylor series expansion of Eq. (1) up to the cubic term is no longer applicable for highly squinted SAR imaging; however, Taylor series expansion (1) up to the quartic term, namely, the fourth-order phase model (FoPM), should be considered to increase the accuracy of the algorithm in the final focusing.

3 Improved SPECAN imaging algorithm

The flowchart of the imaging algorithm is shown in Fig. 3. The left part is the traditional SPECAN algorithm, where H_{RC}, H_{LRWC}, and H_{AC} represent the range compression (RC) function, the linear range walk correction (LRWC) function, and the azimuth compression (AC) function, respectively. The related details were previously reported [16]. The procedure of the improved imaging algorithm is shown in the right part of Fig. 3, which mainly includes Doppler centroid, ASLD correction, and range processing. Each step is discussed in detail below.

3.1 Preprocessing

In squinted SAR processing, the squint angle causes a nonzero Doppler centroid [23–25]. To remove the effect of the squint angle, the Doppler center should first be shifted.

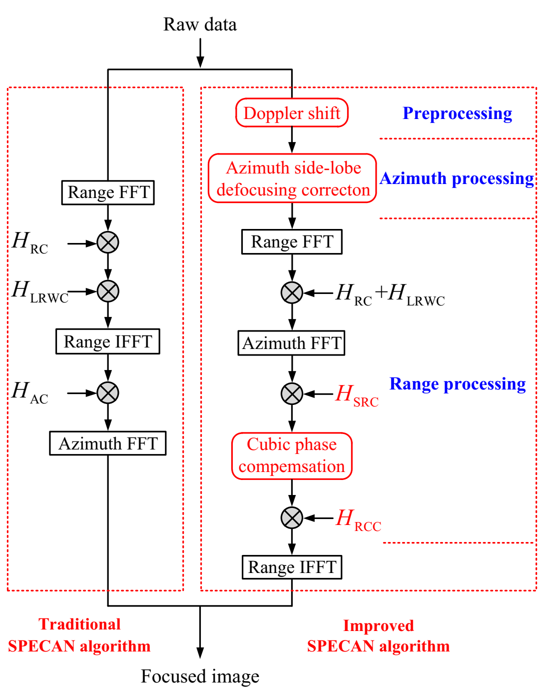

Fig. 3 Comparison of the traditional and improved SPECAN algorithms

3.2 Azimuth processing

In azimuth processing, we adopted the FoPM for the azimuth phase to eliminate the ASLD phenomenon. The fourth-order ASLD correction function is

$$H_{\mathrm{ASLDC}} = \exp\left\{ j4\pi f_{\mathrm{c}} \frac{\left[\gamma_1(R_{\mathrm{c}})t_{\mathrm{a}} + \gamma_2(R_{\mathrm{c}})t_{\mathrm{a}}^2 + \gamma_3(R_{\mathrm{c}})t_{\mathrm{a}}^3 + \gamma_4(R_{\mathrm{c}})t_{\mathrm{a}}^4\right]}{\mathrm{c}} \right\} \tag{9}$$

Then, the fourth-order ASLD correction function is multiplied by the preprocessed echo data. Up to now, the Doppler spectrum was shifted to its own Doppler center, and the ASLD phenomenon was eliminated as well.

3.3 Range processing

This subsection describes how the range-focusing problem of highly squinted echo signals can be solved using the following three steps.

3.3.1 Range compression

By applying the range fast Fourier transform (FFT) to transform the echo signal into the range frequency domain, the signal becomes

$$S_{\mathrm{s}}\left(t_{\mathrm{a}}, f_{\mathrm{r}}\right) = A\sigma(\theta_{\mathrm{i}}, \theta_{\mathrm{a}}) \exp\left(-j\pi \frac{f_{\mathrm{r}}^2}{K_{\mathrm{r}}}\right) \exp\left[-j4\pi\left(f_{\mathrm{r}} + f_{\mathrm{c}}\right)\frac{R(t_{\mathrm{a}})}{c}\right] \tag{10}$$

where f_{r} is the range frequency. A is the constant term and the weighted factors unrelated to the imaging algorithm processing.

Observing (10), the RC can be completed by multiplying (10) with the following RC function:

$$H_{\mathrm{RC}} = \exp\left(j\pi \frac{f_r^2}{K_r}\right) \tag{11}$$

For further convenient analysis, we analyzed the impact of squint angle varying from 0° to 80° on LRW R_{walk} and range curvature R_{curve} based on Eq. (3) and Table 1, which are shown in Fig. 4a, b. For a side-looking SAR with a squint angle of zero, the range walk is zero. In this case, the total RCM only contains the range curvature. However, for a squint SAR, due to the squint angle, the total RCM only contains the component of range curvature, but

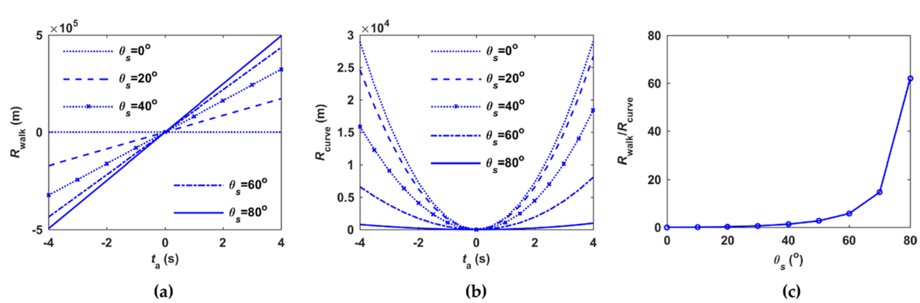

Fig. 4 Simulation results for different squint angles: **a** LRW R_{walk}, **b** range curvature R_{curve}. **c** The ratio of LRW to range curvature $R_{\mathrm{walk}}/R_{\mathrm{curve}}$

also the component of range walk. To quantitatively analyze the ratio of LRW to range curvature $\frac{R_{\text{walk}}}{R_{\text{curve}}}$, Fig. 4c depicts the simulation results and the system parameters are shown in Table 1. The ratio increases with the squint angle. Furthermore, for a higher squint angle, the LRW component becomes the dominant part of the total RCM, but the range curvature is extremely small. Accordingly, the LRWC operation is particularly important in the entire RCMC for the highly squinted SAR. Once the LRW is removed, only a small amount of range curvature remains, which is much easier to correct.

3.3.2 Linear range walk correction

According to the above analysis, substituting Eqs. (3) into (10), the corresponding LRW removal function is:

$$H_{\text{LRWC}} = \exp\left[j4\pi\left(f_r + f_c\right)\frac{\gamma_1(R_c)}{c}t_a\right] \tag{12}$$

The echo data after the LRWC are expressed as:

$$S_s\left(t_a, f_r\right) = A\sigma\left(\theta_i, \theta_a\right)\exp\left[-j4\pi\left(f_r + f_c\right)\frac{R'(t_a)}{c}\right] \tag{13}$$

where $R'(t_{\text{a}}) = R_{\text{c}} + \gamma_2(R_{\text{c}})t_{\text{a}}^2 + \gamma_3(R_{\text{c}})t_{\text{a}}^3 + \gamma_4(R_{\text{c}})t_{\text{a}}^4$. Up to now, the LRW was removed, which considerably mitigated the cross-coupling between the range and azimuth directions.

3.3.3 Secondary range compression and range curvature correction

Then, transforming Eq. (13) into the 2D frequency domain by azimuth FFT with the principle of stationary phase (POSP), we obtain

$$\begin{aligned} S_s\left(t_a, f_r\right) = {} & A\sigma\left(\theta_i, \theta_a\right)\cdot\exp\left\{-j\frac{4\pi\left(f_r + f_c\right)R_c}{c}\right\} \\ & \cdot\exp\left\{-j\frac{\pi R_c c}{2v^2\cos^2\theta_s\left(f_r + f_c\right)}f_a^2\right\} \\ & \cdot\exp\left\{-j\frac{\pi R_c c^2\sin\theta_s}{4v^3\cos^4\theta_s\left(f_r + f_c\right)^2}f_a^3\right\} \\ & \cdot\exp\left\{-j\frac{\pi R_c c^3\left(5\sin^2\theta_s - 1\right)}{32v^4\cos^6\theta_s\left(f_r + f_c\right)^3}f_a^4\right\} \end{aligned} \tag{14}$$

Then, we can expand it into a Taylor series with respect to f_{r}, it is:

$$\begin{aligned} S_s\left(f_{\text{a}}, f_{\text{r}}\right) = {} & A\sigma\left(\theta_{\text{i}}, \theta_{\text{a}}\right) \\ & \cdot\exp\left\{\text{j}\left[\phi_0\left(f_{\text{a}}\right) + \phi_1\left(f_{\text{a}}\right)f_{\text{r}} + \phi_2\left(f_{\text{a}}\right)f_{\text{r}}^2 + \phi_3\left(f_{\text{a}}\right)f_{\text{r}}^3 + \cdots\right]\right\} \end{aligned} \tag{15}$$

where $\phi_0\left(f_{\text{a}}\right)$, $\phi_1\left(f_{\text{a}}\right)$, $\phi_2\left(f_{\text{a}}\right)$, and $\phi_3\left(f_{\text{a}}\right)$ are the respective coefficients of each expansion term; the second term is the range curvature term; and the third term is the quadratic function of f_{r}. The range and azimuth directions are strongly coupled, which substantially complicates the processing of squint SAR echoes [26]. To remove this effect, the secondary range compression (SRC) operation should be implemented. Due to the high squint angle, the influence of cubic phase term in (15) cannot be ignored; otherwise, it will result in an asymmetrical side lobe in the range direction. Hence, before the RCC operation, a precise compensation for the SRC and the cubic phase term must be performed. The corresponding compensation factor is described by:

$$H_{\text{SRC+Cubic+RCC}} = \exp\left\{-\mathrm{j}\left[\phi_1(f_{\mathrm{a}})f_{\mathrm{r}} + \phi_2(f_{\mathrm{a}})f_{\mathrm{r}}^2 + \phi_3(f_{\mathrm{a}})f_{\mathrm{r}}^3\right]\right\} \tag{16}$$

Multiplying (15) with (16) and the final focused SAR images can be obtained by inverse FFT in the range direction.

4 Simulation experiments and discussions

To validate the effectiveness and feasibility of the proposed algorithm on processing highly squinted SAR echoes, we conducted some simulation experiments with a squint angle of 80°. All the simulation parameters were the same as those listed in Table 1.

4.1 Simulation of point targets

Figure 5 depicts the geometrical distribution of point target positions, where A is the near point, B is the scene center point, and C is the far point. In this simulation, we assumed the backscattering coefficients of the three points were 1.

The focused SAR images of targets A, B, and C are shown in Fig. 6. We obtained the images shown in Fig. 6a, b using the traditional [16] and improved SPECAN algorithms, respectively. A comparison of the images in Fig. 6a, b shows that an ideal symmetrical cross-shape is presented in each figure in Fig. 6b, whereas the images in Fig. 6a show asymmetry in the azimuth direction. A comparison of the results further shows that the traditional imaging algorithm cannot achieve satisfactory imaging results with a higher squint angle. In addition, for a longer distance, SAR images are still focused well in Fig. 6b, which indicates that the spatial-variant RCM was well-corrected. The simulation results showed that the proposed method performs better than the traditional method in processing highly squinted SAR echoes.

To further verify the advantages provided by the improved SPECAN algorithm, we depict the results of the comparison of the profiles from the center of the simulated

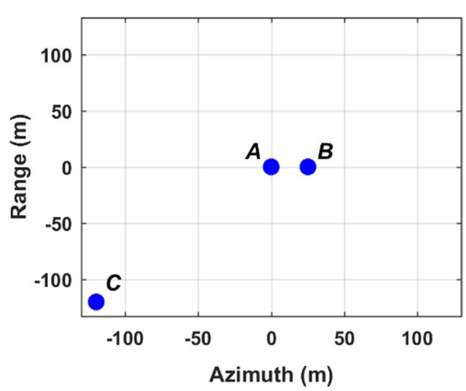

Fig. 5 Geometrical distribution of target positions

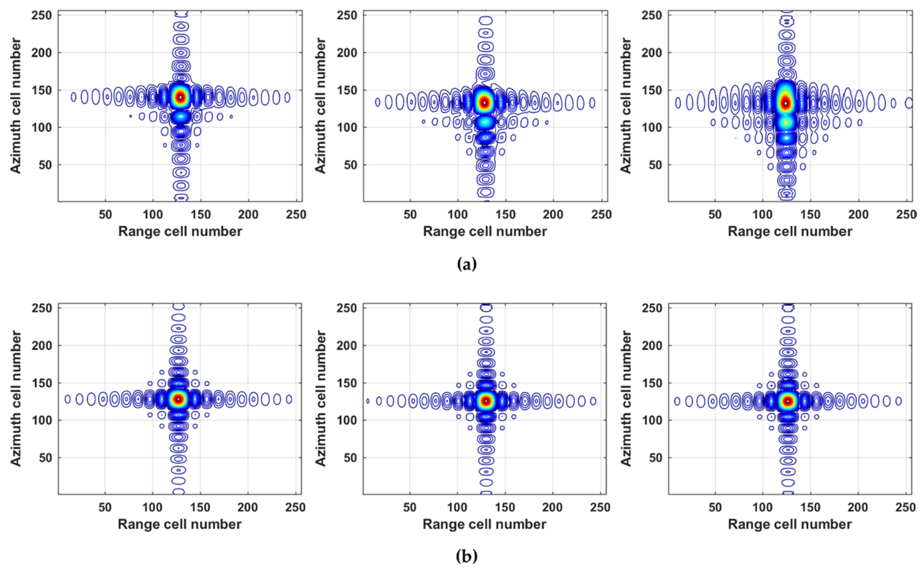

Fig. 6 Contour plot processed by different imaging algorithms. The subfigures from left to right in each row are the images of point *A*, *B*, and *C*, respectively: **a** traditional SPECAN algorithm. **b** Improved SPECAN algorithm

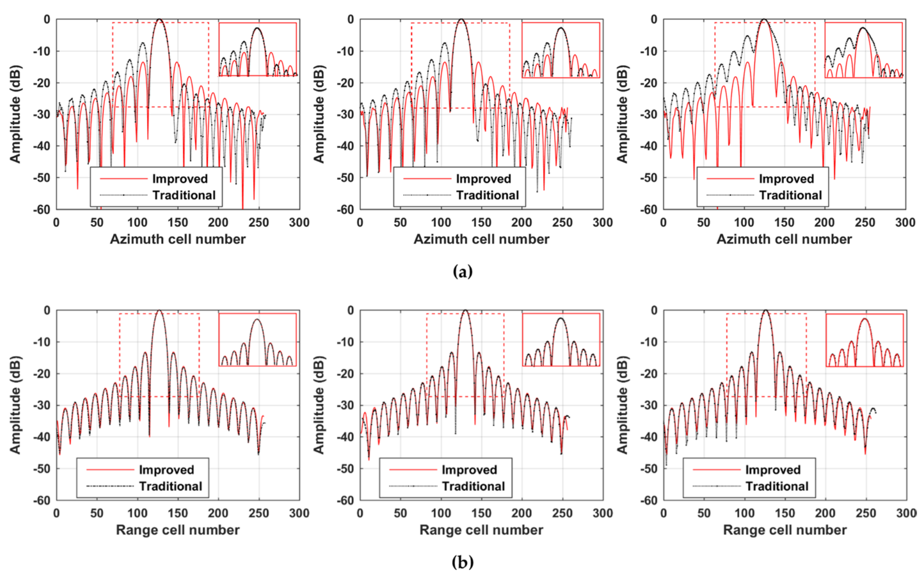

Fig. 7 Comparison of the results of the profiles in different directions obtained by the traditional and improved SPECAN algorithms. The subfigures from left to right in each row correspond to the scattering point *A*, *B*, and *C*, respectively: **a** azimuthal profile. **b** Range profile

images in different directions by the traditional and improved SPECAN algorithm in Fig.7. Figure 7a, b depicts the azimuthal profiles and the range profiles, respectively. The azimuthal side lobe obtained by the traditional SPECAN algorithm is asymmetrical due to the inaccurate azimuthal spectrum. In contrast, when using the improved SPECAN algorithm, the ASLD is eliminated based on the accurate FoPM. Likewise, the magnitudes of azimuth slices indicate that these point targets are well-focused.

We adopted the peak side-lobe ratio (PSLR) as the criterion to evaluate the performance of the improved algorithm. The PSLR values corresponding to the six images in Fig. 7 are listed in Table 2. The PSLR values in azimuth direction generated with the improved method are much lower than those obtained with the original SPECAN method. The numerical results indicate that the PSLRs of the point targets in both the azimuth and range directions obtained by the improved algorithm all meet the requirements of SAR systems [27]. Together with the above comparison results, we found that the improved SPECAN algorithm can substantially improve the azimuthal side-lobe characteristics of SAR imaging results compared with those of the traditional SPECAN algorithm at higher squint angles.

4.2 *SAR* image simulation of targets

We further verified the performance of the proposed algorithm by simulating SAR images of a complex airplane target and a composite ship-ocean scene. SAR echo of the airplane target and the composite ship-ocean scene were generated based on Equation (2). The main procedures can be summarized as below.

Step 1 Divided the SAR imaging scene into triangle patches.

Step 2 For an azimuth sampling time, calculate the radar cross sections of each patch based on the electromagnetic scattering model. In this study, we adopted the geometrical optics and physical optics (GO-PO) method [19] to calculate the scattering coefficients of the airplane, and the combination of the facet-based asymptotical model [28] and GO-PO method to calculate the RCS of each facet.

Step 3 For an azimuth sampling time, calculate the radar echo based on Eq. (2).

Step 4 Repeat the above two step to generate SAR echo for each azimuth sampling time.

Step 5 Apply the proposed improved SPECAN method to the echo to obtain focused SAR image.

4.2.1 SAR imaging simulation of a complex airplane target

For further application, we simulated the highly squinted SAR image of an airplane shown in Fig. 8 using the improved SPECAN algorithm under a squint angle of 80°. Figure 8a displays the geometrical model of an airplane. In this simulation, the SAR platform worked in VV mode and flied along the positive y direction; the simulation parameters were the same as those listed in Table 1.

Table 2 PSLR of three point targets

Squint angle (°)	Target	Traditional SPECAN algorithm		Improved SPECAN algorithm	
		PSLR (dB)		PSLR (dB)	
		Azimuth	Range	Azimuth	Range
80	*A*	−7.44	−13.42	−13.50	−13.27
	B	−7.43	−13.41	−13.47	−13.25
	C	−5.34	−13.27	−13.38	−13.23

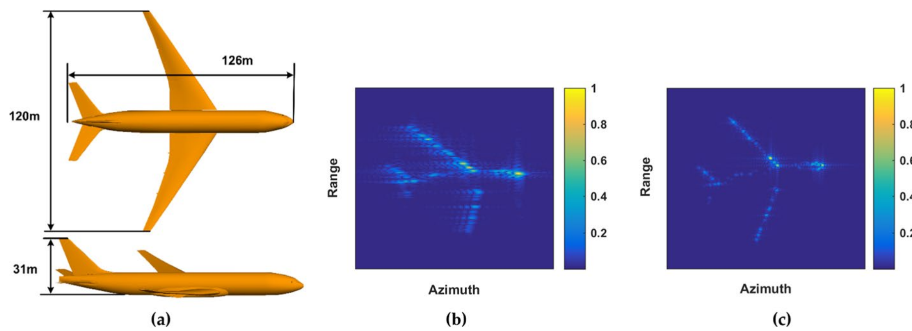

Fig. 8 SAR imaging simulation of an airplane: **a** geometrical model of an airplane. **b** SAR image of the airplane produced by the traditional SPECAN algorithm. **c** SAR image of the airplane produced by the improved SPECAN algorithms

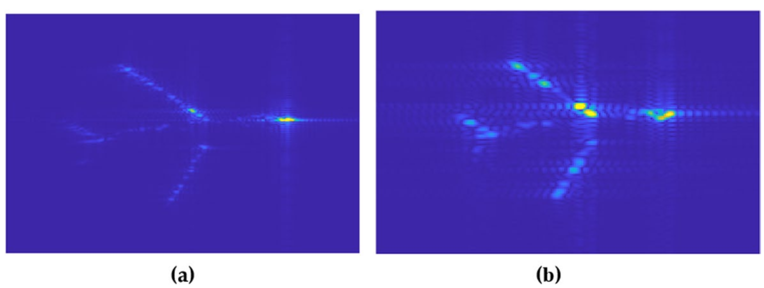

Fig. 9 SAR imaging simulation of an airplane: **a** The radar central frequency is 5 GHz. **b** The radar bandwidth is changed to 40 MHz

Figure 8b, c depicts the SAR images of a complex airplane target simulated using the traditional and improved SPECAN algorithms, respectively. We normalized the intensity of the SAR image with its maximum value. The defocus phenomenon appears in Fig. 8b, while it disappears in Fig. 8c, showing that the improved SPECAN algorithm produces higher-quality results when dealing with highly squinted SAR echoes. In addition, from the SAR image simulated by the improved algorithm, we observed that the plane body, the wings, and the empennage were clearly displayed. Additionally, even in high-squint mode, the simulated SAR image clearly shows the geometry structure of the airplane target.

Moreover, we changed the radar frequency and the bandwidth to further show the good performance of the proposed method under different conditions. In Fig. 9a, the radar central frequency is changed to 5GHz, while other parameters remain. It is seen that the plane body, the wings, and the empennage were still clearly displayed. However, the strong scattering centers are not the same with that in Fig. 8b, which was caused by the different frequency. In Fig. 9b, the radar bandwidth is changed to 40MHz; the resolution decreases compared with Fig. 8b.

Furthermore, the signal-to-noise ratio (SNR) is considered. The amplitude of SAR echo is shown in Fig. 10a with a SNR of 15dB; the corresponding SAR image is shown in Fig. 10b. The simulation parameters are the same with Fig. 8. The simulation results indicate the good performance of the proposed method in real case.

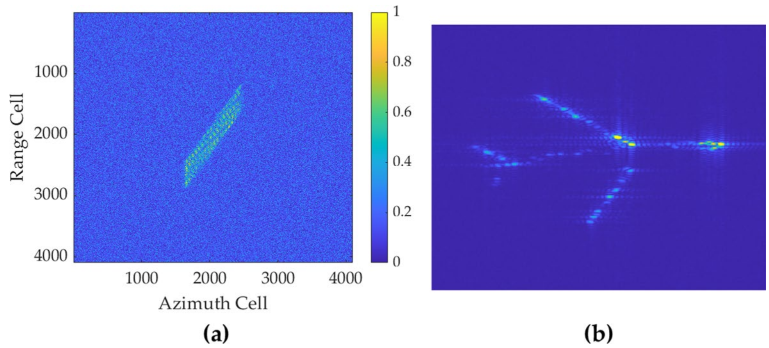

Fig. 10 **a** SAR echo amplitude. **b** SAR image of the airplane with a SNR of 15 dB

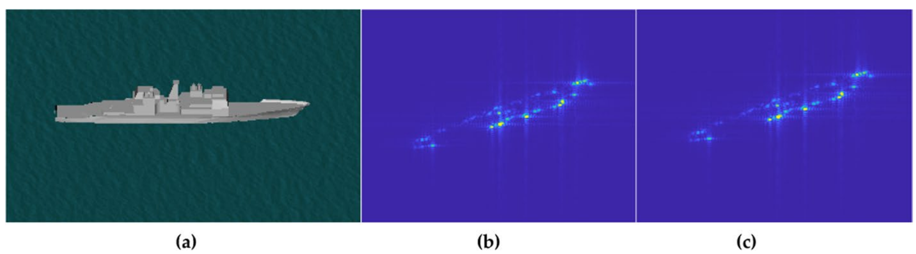

Fig. 11 SAR imaging simulation of a composite ship-ocean scene: **a** geometrical model of the scene. **b** SAR image without noise. **c** SAR image with a SNR of 15 dB

4.2.2 SAR imaging simulation of a composite ship-ocean scene

In this section, we simulated the highly squinted SAR image of a composite ship-ocean scene in Fig. 11 using the improved SPECAN algorithm under a squint angle of 80°. Figure 11a is the geometrical model of the composite ship-ocean scene. The simulated SAR images are illustrated in Fig. 11b, c, there was no noise for Fig. 11b, and the SNR is set as 15 dB for Fig. 11c. Other parameters are shown in Table 1.

From the simulated SAR images, we can see the well-focused ship target. However, the ocean disappears in SAR images. The reason is that for a large incidence angle, the radar echo is much weaker than that of the ship target.

5 Conclusions

In this study, we constructed an improved fourth-order SPECAN algorithm for processing highly squinted SAR echoes. Compared with the traditional SPECAN algorithm, the high-order terms of the range equation are maintained in FoPM, which is helpful for solving problems including ASLD and spatial-variant RCM in high-squint mode. In addition, the efficiency of the proposed method is high because the procedures of the improved SPECAN algorithm only involve FFT and complex multiplication. On this basis, we conducted some simulation experiments to test the performance of the improved SPECAN algorithm, and the imaging results demonstrated that the proposed method performs better than the original imaging algorithm. Additionally, through the simulated SAR images of a complex airplane target and a composite ship-ocean scene, we further verified the ability of the improved SPECAN algorithm to simulate and analyze highly squinted SAR images. All the numerical analyses showed that the proposed algorithm is of theoretical interest and relevant to applications in target identification and detection. In the future, we will carry out airborne flight experiments to further verify and optimize the SAR echo processing method.

Author contributions

WF and MZ conceptualized the study; WF helped in methodology, investigation, writing—original draft preparation, and writing—review and editing; WF and YB validated the study; all authors have read and agreed to the published version of the manuscript.

Funding

This work was supported by the National Natural Science Foundation of China under Grant Nos. 62201443 and 12004293, the Scientific Research Program Funded by Shaanxi Provincial Education Department Program under Grant No. 22JK0427, and the Research Foundation of Xi'an Aeronautical Institute under Grant No. 2020KY0207.

Data availability

Not applicable.

Declarations

Competing interests

The authors declare no conflict of interest.

Received: 25 October 2023 Accepted: 8 March 2024
Published online: 18 March 2024

References

1. L.D. Robertson, A. Davidson, H. Mcnairn, M. Hosseini, M.H. Cosh, Synthetic aperture radar (SAR) image processing for operational space-based agriculture mapping. Int. J. Remote Sens. **41**(18), 7112–7144 (2020)
2. Y.J. Yang, S. Singha, R. Mayerle, A deep learning based oil spill detector using sentinel-1 SAR imagery. Int. J. Remote Sens. **43**(11), 4287–4314 (2022)
3. R. Cao, Y. Wang, S.B. Sun, Y. Zhang, Three dimension airborne SAR imaging of rotational target with single antenna and performance analysis. IEEE Trans. Geosci. Remote Sens. **60**, 5225417 (2022)
4. S. Perna, C. Esposito, P. Berardino, A. Pauciullo, C. Wimmer, R. Lanari, Phase offset calculation for airborne InSAR DEM generation without corner reflectors. IEEE Trans. Geosci. Remote Sens. **53**(5), 2713–2726 (2015)
5. Q. Felipe, M. Younis, G. Krieger, A. Moreira, An analytical error model for spaceborne SAR multichannel azimuth reconstruction. IEEE Geosci. Remote Sens. Lett. **15**(6), 853–857 (2018)
6. N.G. Jiao, F. Wang, H.J. You, X.L. Qiu, Geolocation accuracy improvement of multi-observed GF-3 spaceborne SAR imagery. IEEE Geosci. Remote Sens. Lett. **17**(10), 1747–1751 (2020)
7. L.J. Zhang, Y.S. Gao, X.Z. Liu, Adaptive reconstruction for azimuth signal of multichannel HRWS SAR imaging system. EURASIP J. Adv. Signal Process. **40**, 1–19 (2018)
8. P. Wei, J.J. Wu, Y.L. Huang, J.Y. Yang, Squinted airborne synthetic aperture radar imaging with unknown curved trajectory. Sensors **20**(21), 6026 (2020)
9. X. Zhu, P. Huang, W. Xu, W. Tan, Y. Qi, A modified keystone-based forward-looking arc array synthetic aperture radar 3D imaging method. Sensors **23**(5), 2674 (2023)
10. P. Wei, Y.L. Huang, J.J. Wu, J.Y. Yang, W.C. Li, A residual range cell migration correction algorithm for bistatic forward-looking SAR. EURASIP J. Adv. Signal Process. **110**, 1–12 (2016)
11. A.M. Smith, A new approach to range-Doppler SAR processing. Int. J. Remote Sens. **12**(2), 235–251 (1991)
12. R.K. Raney, H. Bamler, I.G. Cumming, F.H. Wong, Precision SAR processing using chirp scaling. IEEE Trans. Geosci. Remote Sens. **32**(4), 786–799 (1994)
13. G.W. Davidson, I.G. Cumming, M.R. Ito, A chirp scaling approach for processing squint model SAR data. IEEE Trans. Aerosp. Electron. Syst. **32**(1), 121–133 (1996)
14. G.G. Liu, L.R. Zhang, N. Liu, G.F. Chen, Y. Zhang, Focusing highly squinted data using the extended nonlinear chirp scaling algorithm. IEEE Geosci. Remote Sens. Lett. **10**(2), 342–346 (2013)
15. M. Liang, W.M. Su, C. Ma, H. Gu, J.C. Yang, Focusing one-stationary bistatic forward-looking synthetic aperture radar based on squint minimization and modified nonlinear chirp scaling algorithm. Int. J. Remote Sens. **39**(21/22), 7830–7845 (2018)
16. G. Zhang, L.B. Yang, M.B. Zhu, X.P. Li, SPECAN imaging algorithm for missile-borne SAR with high squint angle. Radio Eng. **42**(11), 10–13 (2012)
17. G. Hu, X. Ye, X. Hu, Y. Tang, A novel method for squint SAR image reconstruction and graphic correction based on the SPECAN algorithm, in *IEEE Conference on Industrial Electronics and Applications*, Melbourne, Australia, pp. 640–645 (2013).
18. W.B. Gordon, Far-field approximation to the kirchhoff-helmholtz representation of the scattered fields. IEEE Trans. Antennas Propag. **23**, 590–592 (1975)

19. P.B. Wei, M. Zhang, W. Niu, W.Q. Jiang, GPU-based combination of GO and PO for electromagnetic scattering of satellite. IEEE Trans. Antennas Propag. **60**(11), 5278–5285 (2012)
20. C. Özdemir, B. Yilmaz, Ö. Kirik, pRediCS: a new GO-PO-based ray launching simulator for the calculation of electromagnetic scattering and RCS from electrically large and complex structures. Turk. J. Electr. Eng. Comput. Sci. **22**(5), 1255–1269 (2015)
21. X. Sun, T.S. Yeo, C. Zhang, Y. Lu, S.K. Pang, Time-varying step-transform algorithm for high squint SAR imaging. IEEE Trans. Geosci. Remote Sens. **37**(6), 2668–2677 (1999)
22. T.S. Yeo, N.L. Tan, C.B. Zhang, Y.H. Lu, A new subaperture approach to high squint SAR processing. IEEE Trans. Geosci. Remote Sens. **39**(5), 954–968 (2001)
23. S.X. Zhang, M.D. Xing, X.G. Xia, L. Zhang, R. Guo, Z. Bao, Focus improvement of high-squint SAR based on azimuth dependence of quadratic range cell migration correction. IEEE Geosci. Remote Sens. Lett. **10**(1), 150–154 (2012)
24. D. An, X. Huang, T. Jin, Z. Zhou, Extended two-step focusing approach for squinted spotlight SAR imaging. IEEE Trans. Geosci. Remote Sens. **50**(7), 2889–2900 (2012)
25. X. Wei, Y. Deng, P. Huang, R. Wang, Full-aperture SAR data focusing in the spaceborne squinted sliding-spotlight mode. IEEE Trans. Geosci. Remote Sens. **52**(8), 4596–4607 (2014)
26. G.C. Sun, X.W. Jiang, M.D. Xing, Z.J. Qiao, Y.R. Wu, Z. Bao, Focus improvement of highly squinted data based on azimuth nonlinear scaling. IEEE Trans. Geosci. Remote Sens. **49**(6), 2308–2322 (2011)
27. I.G. Cumming, F.H. Wong, *Digital Processing of Synthetic Aperture Radar Data: Algorithms and Implementation* (Artech House, Norwood, 2005)
28. M. Zhang, Y. Zhao, J.-X. Li, P.-B. Wei, Reliable approach for composite scattering calculation from ship over a sea surface based on FBAM and GO-PO models. IEEE Trans. Antennas Propag. **65**(2), 775–784 (2017)